**PAPER • OPEN ACCESS**

# How does inow veer affect the veer of a wind-turbine wake?

To cite this article: Antonia Englberger and Julie K. Lundquist 2020 *J. Phys.: Conf. Ser.* **1452** 012068

View the article online for updates and enhancements.

Recent citations

- Investigation of Marine Wind Veer Characteristics Using Wind Lidar Measurements
  Zhenru Shu *et al*

# How does inflow veer affect the veer of a wind-turbine wake?

**Antonia Englberger\*, and Julie K. Lundquist\*\* \*\*\***

\*Institut für Physik der Atmosphäre, DLR Oberpfaffenhofen, Germany
\*\*Department of Atmospheric and Oceanic Sciences, University of Colorado Boulder, Boulder, Colorado, USA
\*\*\*National Renewable Energy Laboratory, Golden, Colorado, USA

E-mail: `antonia.englberger@dlr.de`, `julie.lundquist@colorado.edu`

**Abstract.** Stably stratified flow conditions often exhibit wind veer, or a change of wind direction with height. When wind turbines experience this veered flow, the resulting wake structure tends to exhibit a stretching into an ellipsoid, rather than a symmetric shape or a curled shape. Observational studies suggest that the magnitude of wake veer is less than the veer of the inflow, whereas large-eddy simulations with actuator disk models and actuator line models suggest a range of relationships between inflow veer and wake veer. Here we present a series of large-eddy simulations with a range of veer shapes, a range of magnitudes of veer, a range of wind speeds, and both rotational directions of the wind-turbine rotor investigating the effect on the wake deflection angle. These results can guide the application of wake steering in stably stratified flow.

## 1. Introduction

The atmospheric boundary layer over land experiences a diurnal cycle in atmospheric stability driven by the changing role of surface heating. During the daytime, shortwave heating of the surface triggers convective turbulence that mixes throughout the boundary layer, resulting in high levels of turbulence and a well-mixed boundary layer with little wind shear [1]. In contrast, at night, the decay of this convective turbulence results in low ambient levels of turbulence and a highly sheared wind profile that can include nocturnal low-level jets. Many of the worlds regions of large wind resources such as the US Great Plains owe their large wind resource to these nocturnal low-level jets [2].

Just as wind speed tends to increase with height during these stably stratified conditions, wind direction also tends to change with height. This change of wind direction with height, or veer, reflects the change in the balance of forces with altitude: near the surface, turbulent stresses are larger and flow tends to be directed towards low pressure regions, In contrast, further aloft, turbulent stresses are smaller and flow approaches geostrophic flow, flowing along constant pressure levels. This rotation of the winds with height is referred to a directional shear or veer. Meteorologists distinguish clockwise rotation with height, veering [1], from counterclockwise rotation with height, backing. Veering tends to be associated with warm air advection while backing is associated with cold air advection. Observations in Texas [3], Iowa [4], and off the coast of Massachusetts [5] all indicate that veer in excess of $0.2\,^\circ\,\mathrm{m}^{-1}$ can be expected in stably

stratified conditions. The profile of veer is not necessarily linear, and can take a variety of shapes depending on surface drag, geostrophic forcing, and other conditions.

Wake veer, or the stretching of a wind-turbine wake, can be calculated by comparing the center line of the wake at the bottom tip to the center line of the wake at the top tip. Observations of wake veer, based on lidar estimates of the wake result in a smaller magnitude of wake veer in comparison to the veer of the inflow [6]. In contrast, large-eddy simulations (LESs) with actuator disk models [7, 8, 9] and actuator line models [8] suggest only a minor difference between inflow veer and wake veer (Fig. 1a). The actuator line model results with SOWFA [10, 11, 12] lie between the observations and the other modelling studies. In this work, we evaluate the relation between inflow veer and the veer of a wind-turbine wake by testing a range of veer shapes, magnitudes of veer, and hub height wind speeds using the LES model EULAG with an actuator disc parametrization of the wind-turbine rotor.

## 2. Data and Methods

The stably stratified atmospheric boundary layer flow interacting with a wind turbine is simulated with the multiscale geophysical flow solver EULAG [13]. The model integrates the non-hydrostatic Boussinesq equations of motion and continuity

$$\frac{d\mathbf{v}}{dt} = -G\boldsymbol{\nabla}\left(\frac{p^{'}}{\rho_0}\right) + \mathbf{g}\frac{\Theta^{'}}{\Theta_0} + \frac{\mathbf{F}}{\rho_0},$$

$$\frac{d\Theta^{'}}{dt} = -\mathbf{v}\nabla\Theta_e,$$

$$\boldsymbol{\nabla} \cdot (\rho_0 \mathbf{v}) = 0,$$

and solves for the Cartesian velocity components $\mathbf{v} = (u, v, w)$ and the potential temperature perturbation $\Theta^{'}$, for a flow with constant density $\rho_0 = 1.1 \, \mathrm{kg \, m^{-3}}$ and a constant reference value $\Theta_0 = 300 \, \mathrm{K}$ [14]. In the set of equations, $d/dt$, $\boldsymbol{\nabla}$, and $\boldsymbol{\nabla} \cdot$ represent the total derivative, the gradient, and the divergence, respectively. The factor $p^{'}$ represents the pressure perturbation with respect to the background density, and $\mathbf{g}$ is the vector of acceleration due to gravity. The metric coefficients $G$ represents geometric terms that result from the general, time-dependent coordinate transformation. $\mathbf{F}$ is the turbine-induced force in the wind-turbine simulations. They are parameterized with the blade element momentum method as rotating actuator disc including a nacelle [15]. The simulated wind turbine has a diameter $D$ and a hub height $z_h$ of 100 m.

We performed idealized LESs on $512 \times 64 \times 64$ grid points with a horizontal and vertical resolution of 5 m and with three different shapes of veer. These types of veer include linear veer limited only to the lower half of the rotor (bot_veer), linear veer over the entire rotor (full_veer), and linear veer over only the top half of the rotor (top_veer). When veer is present, it is defined to be 0.16 ° m$^{-1}$ over the corresponding rotor part following Eq. (1).

$$\phi_{wind_{full\_veer}}(z) = 254° + 0.16° \ m^{-1} \cdot z \tag{1}$$

$$\phi_{wind_{full\_veer\_weak}}(z) = 262° + 0.08° \ m^{-1} \cdot z \tag{2}$$

We conducted additional weak veer simulations (full_veer_weak) with 0.08 ° m$^{-1}$ over the corresponding rotor part following Eq. (2). The chosen strength of both veering winds is in agreement with [3, 4, 5]. The wind direction is chosen to result in $v(z_h) = 0$ in all four simulation types with

$$u(z) = u_g \cdot \left(1 - exp\left(-\frac{z\sqrt{f/\kappa}}{\sqrt{2}}\right)\right), \tag{3}$$

with the Coriolis parameter $f = 1.0 \times 10^{-4}$ s$^{-1}$ and an eddy viscosity coefficient $\kappa = 0.06$ m$^2$ s$^{-1}$, following [16]. The geostrophic wind is $u_g = 10$ m s$^{-1}$. In addition, we performed full_veer and full_veer_weak simulations for different $u_g$-values of 6 m s$^{-1}$, 8 m s$^{-1}$, 12 m s$^{-1}$, and 14 m s$^{-1}$. Finally, we performed the full_veer_weak simulation with $u_g = 10$ m s$^{-1}$ for a counterclockwise rotational direction of the actuator disc. The vertical gradient of the potential temperature is 6 K over the lowest 200 m and zero above. In all of these simulations, we apply the parametrization of [17] to represent a turbulent stably stratified regime in a wind-turbine simulation with open horizontal boundary conditions. This parametrization has been successfully used for idealized wind-turbine simulations representing a stable boundary layer regime in [18].

## 3. A veering wind in literature

Figure 1a relates the change in the wind direction angle $\phi_{wind}$ to the change in the wake deflection angle $\phi_{wake}$ over the rotor for various published LES results and compares them with measurements [6]. We consider LESs of the stable or the morning boundary layer of A. Englberger (AE) [9], stable boundary layer regimes of N. Marjanovic (NM) [8] and J. Mirocha (JM) [7], low and moderate stably stratified regimes of K. Bhaganagar (KB) [10], stable regimes of M. Churchfied (MC) [11] and J. Tomaszewski (JT) [12], and lidar measurements of N. Bodini (NB) [6]. The relation of the change over the rotor between $\phi_{wind}$ and $\phi_{wake}$ in Fig. 1a shows striking differences, especially between measurements and simulation results.

**Table 1.** List of the parameters (numerical model, wind-turbine parametrization, resolution, wind veer and wake veer over the rotor (or a certain fraction of it), position of wake veer) of the individual considered LES studies.

| In | abbrev. | num. model | WT param | resol. | $\Delta_D$ wind | $\Delta_D$ wake | pos. of veer |
|------|----------|-------------|-------------|-----------|------------|------------|-------------|
| [9] | AE_SBL | EULAG | ADM | 5 m | 10.1° | 11.3° | lower |
| [9] | AE_MBL | EULAG | ADM | 5 m | 12.5° | 12.0° | lower |
| [8] | NM | WRF-LES | ADM + ALM | 6 m + 2 m | ≈9° | ≈9° | rotor |
| [7] | JM | WRF-LES | ADM | 6 m | ≈5.2° | ≈6.4° | rotor |
| [10] | KB_ls | SOWFA | ALM | 0.75 m | 21.05° | 17.5° | rotor |
| [10] | KB_ms | SOWFA | ALM | 0.75 m | 32.5° | 31.8° | lower |
| [11] | MC | SOWFA | ALM | 1.25 m | 8° | 6.4° | rotor |
| [12] | JT | SOWFA | ALM | 1.25 m | ≈11° | ≈8° | rotor |

As a first step, we investigate the spread of LES results. The relation between the veering wind $\phi_{wind}$ and $\phi_{wake}$ is investigated for the following factors:

- Numerical resolution
- Wind-turbine parametrization (actuator disc method (ADM) vs. actuator line method (ALM))
- Numerical model (SOWFA (OpenFOAM), WRF-LES, EULAG)

In Table 1, the most relevant parameters are listed, which differ in the considered studies. From Table 1, we can exclude a dependence on wind-turbine parametrization or the numerical resolution, as the simulations of [8], performed with an ADM and an ALM parametrization and likewise for 6 m and 2 m resolution, show no differences in the wake deflection angle. In Fig. 1a, the numerical model results of EULAG and WRF-LES are rather similar and in the vicinity of the 1:1 line. The results of SOWFA are following the gray dashed line assuming $\phi_{wake} = 0.8\, \phi_{wind}$ [11]. Therefore, the deviation between SOWFA and EULAG/WRF-LES seems
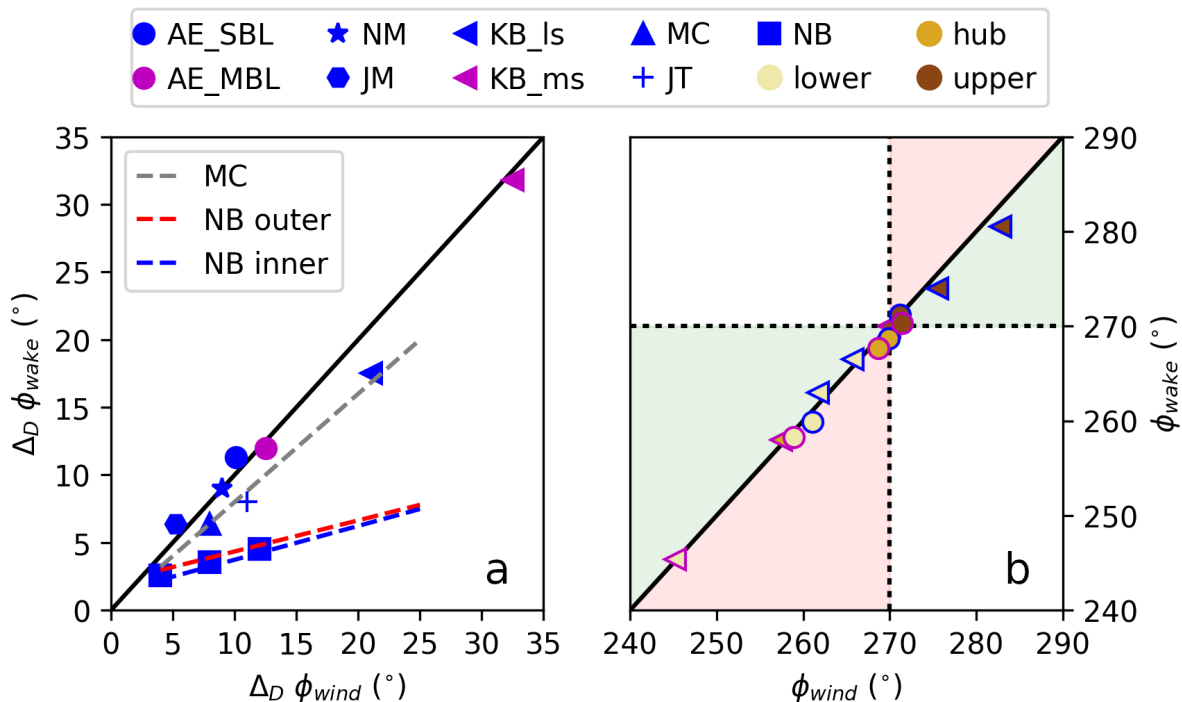
**Figure 1.** Relation between wind direction and wake deflection averaged over the rotor (or a fraction of the rotor) with a diameter $D$ in $a$ and the relation between wind direction and wake deflection at individual heights in the lower and the upper rotor part and also at hub height in $b$. The abbreviations correspond to the following studies of: AE [9] for the stable (SBL) and the morning (MBL) boundary layer wind-turbine simulation, KB [10] for the low (ls) and moderate (ms) stably stratified regime, NM [8], JM [7], MC [11], JT [12], NB [6]. Magenta colors correspond to a more stable regime in comparison to blue contours. Further, the brown shades refer to different vertical heights (lower rotor part, hub height, upper rotor part). The dashed lines in $a$ corresponds to fits from MC [11], and the outer and inner wind-turbine fits from NB [6].

to depend on the numerical model. However, also the gray dashed line differs from the fit on the lidar measurements from NB [6]. Concluding, the numerical model is the reason for the difference between EULAG / WRF-LES results in comparison to SOWFA results.

Further, KB_ms is closer to the 1:1 line as to the gray dashed fitting curve, whereas KB_ls has a perfect fit to this curve (Fig. 1$a$). One major difference between KB_ms and KB_ls is the vertical extension of veer in the operating height of the rotor. In KB_ms a veering wind affects only the lower rotor part, whereas in KB_ls it interacts with the whole rotor, similar to MC [11] and JT [12]. Therefore, another possible impact factor on $\phi_{wake}$ could be the vertical position of the veering wind.

To investigate this vertical variability, we distinguish between the lower and the upper rotor part and also hub height in Fig. 1$b$ for KB_ls, KB_ms, AE_SBL, and AE_MBL, where $\phi_{wind} = 270$ ° corresponds to a westerly wind and $\phi_{wake} = 90$ ° to a eastward propagating wake, with $\phi_{wind} = \phi_{wake} + 180$ ° corresponding to the 1:1 line. Here, $\phi_{wind}$ corresponds to $\phi_{wake} + 180$ ° in the lower rotor part (and likewise at hub height) for all four simulations. In the upper rotor part in KB_ls, however, $\phi_{wake} + 180$ ° is 2.3 ° smaller than $\phi_{wind}$. A difference between these two angles occurs only in a simulation where the veering wind expands over

the whole rotor. Due to this sensitivity, we investigate the impact of veering wind parameters (height, strength, speed) on $\phi_{wake}$ with idealized LESs.

## 4. Influences on the relationship between inflow veer and wake veer

### 4.1. Shape of veering wind profiles

The shape and magnitude of the inflow veer determines the relationship between inflow veer and wake veer, partially explaining the conflicting results in the literature. The relation of $\phi_{wake}$-270 $^{circ}$ to $\phi_{wind}$-270 $^{circ}$ is presented in Figure 2a for the three different wind veering conditions bot_veer, full_veer, and top_veer and $u_g = 10$ m s$^{-1}$ for a streamwise distance up to 6 D. Comparing a veering wind which is limited to the lower rotor part (bot_veer) with a veering wind limited to the upper rotor part (top_veer), a striking difference appears in the ratio of $\phi_{wake}$ towards $\phi_{wind}$, defined as ratio of inflow veer to wake veer. For veer only in the lower half of the disc, the ratio is roughly 0.9 up to 6 D, whereas for veer only in the upper half, the ratio is >1 at 1 D and decreases to roughly 1.04 at 6 D. The ratios at 140 m in the top_veer simulation and at 60 m in the bottom_veer simulation are not shown, as $\phi_{wind}$-270 $^{circ}$ approaches zero. When veer extends across the entire rotor disc, $\phi_{wake}$ is smaller than $\phi_{wind}$ in the lower rotor half at 60 m, larger in the upper rotor half at 140 m up to 4 D and approaches $\phi_{wind}$ further downstream at 140 m. The tendencies of the ratio in the upper and the lower rotor half in full_veer correspond to the results from the top_veer and the bot_veer simulations, only with a slightly smaller fraction at both heights.

The entrainment of flow above the rotor disc, which is characterized by different vertical gradients of $\phi_{wind}$ ($\frac{\partial \phi_{wind}}{\partial z}$), explains these differences. When unveered air ($\frac{\partial \phi_{wind}}{\partial z} = 0$) with faster flow is entrained into the lower rotor half of the wake in the bot_veer simulation, it results in $\phi_{wake} < \phi_{wind}$. However, if veered air ($\frac{\partial \phi_{wind}}{\partial z} \neq 0$) with faster flow is entrained into the upper rotor half of the wake in the top_veer simulation, it results in $\phi_{wake} > \phi_{wind}$. This entrainment process also explains $\phi_{wake_{full\_veer}} < \phi_{wake_{bot\_veer}}$ in the lower rotor part, as the vertical gradient of $\phi_{wind}$ is larger in the full_veer case in comparison to the bot_veer case with no veer above hub height. Further, $\phi_{wake_{full\_veer}} < \phi_{wake_{top\_veer}}$ can also be related to the difference in $\frac{\partial \phi_{wind}}{\partial z}$, here in the lower rotor part.

### 4.2. Magnitude of veering wind

The difference between $\phi_{wake}$ and $\phi_{wind}$ changes when the magnitude of the veer changes. Figure 2b compares the impact of the vertical gradient of $\phi_{wind}$ by comparing the full_veer simulation with $\frac{\partial \phi_{wind}}{\partial z} = \frac{8°}{50\ m}$ in each rotor half to the full_veer_weak simulation with $\frac{\partial \phi_{wind}}{\partial z} = \frac{4°}{50\ m}$ in each rotor half, both for $u_g = 10$ m s$^{-1}$. The pronounced smaller wake deflection angle at 60 m in the full_veer case further decreases in the full_veer_weak case. Likewise, for $x > 3$ D, $\phi_{wake}$ at 140 m is smaller in the full_veer_weak case in comparison to the full_veer case and also towards $\phi_{wind}$. Therefore, the difference between $\phi_{wake}$ and $\phi_{wind}$ increases, if the vertical gradient of the veering wind decreases. The resulting difference between $\phi_{wake}$ and $\phi_{wind}$ can also be related to the entrainment process, which is influenced by the strength of $\frac{\partial \phi_{wind}}{\partial z}$ above the rotor.

### 4.3. Speed of veering wind

In addition to the shape and the magnitude of the incoming veering wind, the wind speed exerts an impact on the relationship between $\phi_{wake}$ and $\phi_{wind}$. Both full-veer cases are performed for $u_g$ of 6 m s$^{-1}$, 8 m s$^{-1}$, 10 m s$^{-1}$, 12 m s$^{-1}$, and 14 m s$^{-1}$. The results are plotted in Fig. 2c and d. The trend of larger inflow veer in comparison to the wake veer $\phi_{wind} > \phi_{wake}$ persists in the lower rotor half, resulting in a ratio < 1. This is valid for all tested wind speeds in the full_veer and the full_veer_weak simulations. In the lower rotor half, $\phi_{wake}$ increases with
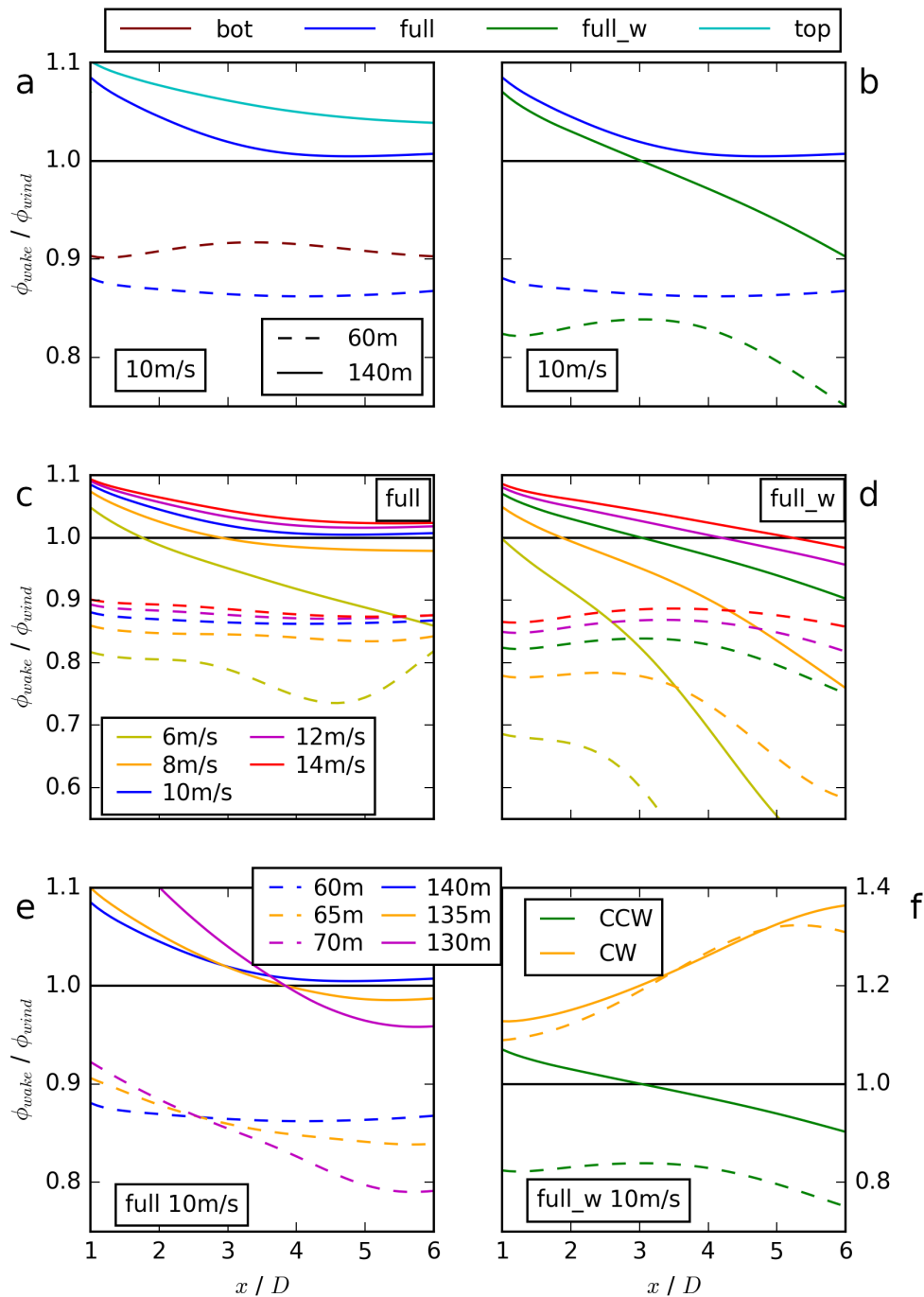
**Figure 2.** Downstream relation of $\phi_{wake}/\phi_{wind}$ for simulations of top_veer (top), full_veer (full), and bot_veer (bot) in $a$, type full_veer and full_veer_weak (full_weak) in $b$, full_veer (full_veer_weak) and $u_g$ of 6 m s$^{-1}$, 8 m s$^{-1}$, 10 m s$^{-1}$, 12 m s$^{-1}$, and 14 m s$^{-1}$ in $c$ ($d$), full_veer_weak and 10 m s$^{-1}$ for various height in the upper and the lower rotor part in $e$, and for counterclockwise rotating wake (CCW) and clockwise rotating wake (CW) for full_veer_weak and 10 m s$^{-1}$ in $f$.

increasing wind speed, resulting in a $ratio_{max} \approx 0.9$ for 10 m s$^{-1}$, 12 m s$^{-1}$, and 14 m s$^{-1}$ in the full_veer simulations, whereas the ratio is still increasing between 12 m s$^{-1}$ and 14 m s$^{-1}$ in the full_veer_weak simulations. The ratio in full_veer_weak also starts to level out at a ratio of 0.9, as the difference between the ratios of 12 m s$^{-1}$ and 14 m s$^{-1}$ is smaller in comparison to the difference between the ratios of 10 m s$^{-1}$ and 12 m s$^{-1}$.

In the upper rotor half, $\phi_{wake}$ also increases with increasing wind speed, approaching $\phi_{wind}$ at $x > 4$ D for all tested wind speeds $\geq 8$ m s$^{-1}$ of the full_veer simulations and approaches towards a slightly smaller ratio value ($< 1$) in the full_veer_weak simulations. Similar to the lower rotor half, $\phi_{wake}$ is larger for a higher wind speed in the upper rotor half, approaching a ratio of 1.0.

Resulting, for high enough wind speeds and a large enough vertical gradient of the veering wind, a maximum wake deflection angle is reached in the upper as well as in the lower rotor half. $\phi_{wake}$ is approximately $\frac{1}{10}$ smaller than $\phi_{wind}$ in the lower rotor half and approaches towards $\phi_{wind}$ in the upper rotor half. This difference in strong wind situations in comparison to weak wind situations can be explained with the entrainment of ambient air, affected by $\phi_{wind}$, with much faster air being mixed into the wake in the strong wind cases.

### 4.4. Radial variation

The impact of the radial position in the upper and the lower rotor part is investigated in Fig. 2e for the simulation full_veer_weak with $u_g = 10$ m s$^{-1}$. There is an impact on the value of the ratio of $\frac{\phi_{wake}}{\phi_{wind}}$, however, the impact is rather small and the trend of the different behaviour between the upper and the lower rotor part persist, verifying the usage of 60 m for a position in the lower rotor part and 140 m referring to the upper rotor part, for a rotor with $z_h = $ D $= 100$ m. The decrease of $\phi_{wake}$ approaching towards the nacelle results from the entrainment of air with a smaller meridional velocity component downstream in the disc region close to the nacelle, in comparison to the outer rotor part, which is much more influenced by the air surrounding the disc with $\phi_{wind}$.

### 4.5. Rotational direction

Studies like [11, 19] suspect that the rotational direction impact $\phi_{wake}$. A clockwise (CW) or a counterclockwise (CCW) rotating near wake, which can be related to counterclockwise (CW) or clockwise (CCW) rotating blades, have a rather strong impact on the ratio of $\phi_{wake}$ and $\phi_{wind}$ (Fig. 2f). Applying counterclockwise rotating blades results in $\phi_{wake} > \phi_{wind}$ in both rotor parts, top and bottom. This increased wake veer can be explained by the linear superposition of rotor-induced vorticity with the veering wind [18].

### 4.6. Relation between $\phi_{wind}$ and $\phi_{wake}$

The wake deflection angle depends on the shape and the magnitude of the veering wind and also its wind speed $u_g$. The ratio of inflow veer to wake veer shows an asymptotic behaviour which is reached in the full_veer case with a large magnitude of veering wind in a strong wind situation. In the upper rotor part, the wake deflection angle aligns with the wind direction, whereas in the lower rotor part, the wake deflection angle is smaller than the wind direction angle, approaching a ratio value of 0.9.

This relation is shown in Fig. 3. Figure 3a corresponds to the third quadrant and Fig. 3b to the first quadrant of Fig. 1b. The green area corresponds to $\phi_{wake} < \phi_{wind}$ and the red area to $\phi_{wake} > \phi_{wind}$. Both angles are rather similar in the upper rotor part with differences $< 0.1$ ° (Fig. 3b), with larger deviations only in the weak wind cases of 6 m s$^{-1}$ and 8 m s$^{-1}$ in full_veer_weak and 6 m s$^{-1}$ in full_veer. In the lower rotor part (Fig. 3a), the differences are much larger. A difference of 0.4 ° occurs in the full_veer_weak simulation with $u_g = 14$ m s$^{-1}$ and of 0.8 ° in the full_veer simulation, also with $u_g = 14$ m s$^{-1}$. The results of the full_veer simulation with $u_g = 14$ m s$^{-1}$ is in a stable end state, as the difference of 0.8 ° also occurs for
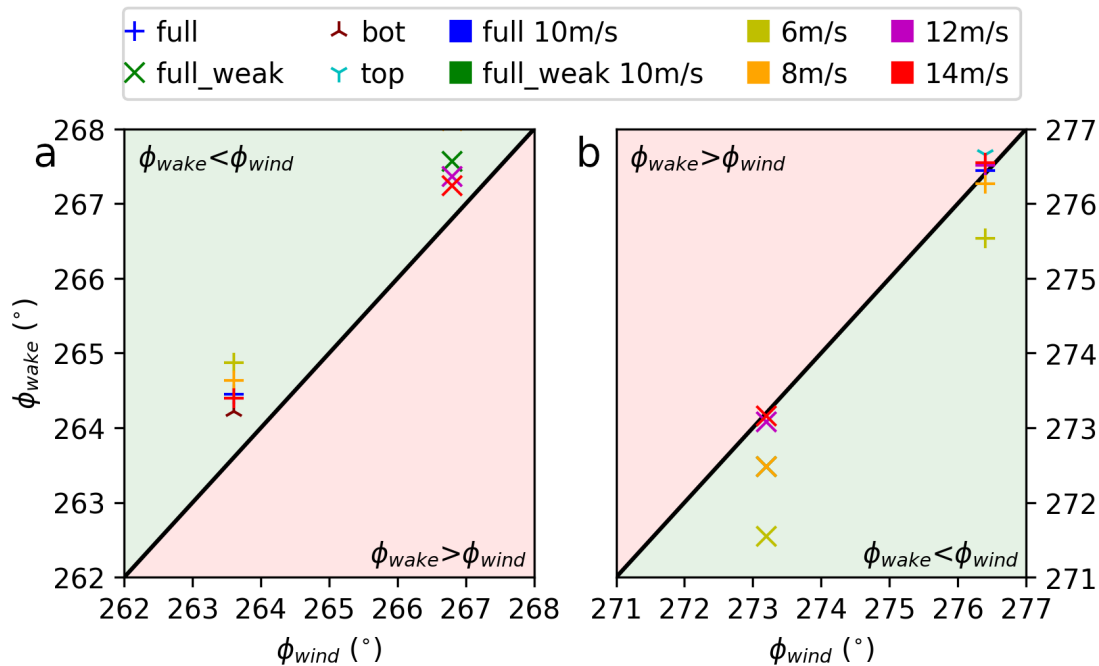
**Figure 3.** Relation of $\phi_{wind}$ towards $\phi_{wake}$ in the lower rotor part in $a$ and the upper rotor part in $b$ for simulations of type bot_veer (bot), top_veer (top), full_veer (full), full_veer_weak (full_weak) and $u_g$ of 6 m s$^{-1}$, 8 m s$^{-1}$, 10 m s$^{-1}$, 12 m s$^{-1}$, and 14 m s$^{-1}$ at a downstream distance of 6 D.

the full_veer simulation with $u_g = 12$ m s$^{-1}$. The full_veer_weak simulation with the same $u_g$ of 14 m s$^{-1}$, however, is still slightly different ($\approx 0.1$ °) from the corresponding full_veer_weak simulation with $u_g = 12$ m s$^{-1}$. Therefore, if the parameters of the veering wind (height, vertical gradient, speed) are large (enough), $\phi_{wake}$ levels out, resulting in $\phi_{wake} < \phi_{wind}$ in the lower rotor part and $\phi_{wake} \approx \phi_{wind}$ in the upper rotor part (red symbols in Fig. 3).

## 5. Discussion and Conclusion

When wind-turbine wakes form in flows with veered wind profiles, the wakes exhibit veer of their own. Results in the literature show a wide variety of relationships between the inflow veer and the wake veer. Using LESs, we explore how the shape and vertical gradient of the veer profile, the magnitude of the inflow wind speed, and the rotational direction of the turbine all impact the veer of the wake, towards resolving the apparent contradictions reported in the literature. Given that wake steering solutions [15] depend on the generation of this veer, the resolution of this question by the present simulations will have immediate impact.

## References

[1]  Stull R. B. 1988 Dordrecht, Kluwer Academic
[2]  Rife D. L. et al 2010 Journal of Climate, 23(19), 5041-5064.
[3]  Walter K et al. 2009 Solar Energy Engineering **131** 011013
[4]  Gomes Sanchez M and Lundquist J K 2019 Wind Energy Science under review
[5]  Bodini N et al. 2019 Geophysical Research Letters **46(10)** 5582-5591
[6]  Bodini N et al. 2017 Atmospheric Measurement Techniques **10(8)** 427-449
[7]  Mirocha N et al. 2015 Journal of Renewable and Sustainable Energy **7(4)** 043143
[8]  Marjanovic N et al. 2017 Journal of Renewable and Sustainable Energy **9(6)** 063308
[9]  Englberger A and Dörnbrack A 2018 Bound. Layer Meteorol. **166** 423-448
[10] Bhaganagar K and Debnath M 2015 Journal of Renewable and Sustainable Energy **7(1)** 013124
[11] Churchfield M J and Sirnivas S 2018 Wind Energy Symposium (p. 0755)
[12] Tomaszewski J M et al. 2018 Wind Energy Science **3(2)** 833-843
[13] Prusa JM et al 2008 Comput. Fluids **37** 1193-1207
[14] Smolarkiewicz PK et al 2007 J. Comput. Physics **227** 633-653
[15] Englberger A and Dörnbrack A 2017 Bound. Layer Meteorol. **162** 427-449
[16] Shapito A and Fedorovich E 2010 Journal of Royal Meteorol. Society. **136** 1255-1262
[17] Englberger A and Dörnbrack A 2018 Bound. Layer Meteorol. **169** 505-536
[18] Englberger A et al 2019 Wind Energy Science Discussion
[19] Vollmer L et al 2016 Wind Energy Science **1** 129-141